Available online at www.sciencedirect.com

ScienceDirect

Soils and Foundations 61 (2021) 798–814

www.elsevier.com/locate/sandf

Technical Paper

A contact model for rough crushable sand

Ningning Zhang [a,b], Matteo O. Ciantia [c,*], Marcos Arroyo [a], Antonio Gens [a]

[a] Department of Geotechnical Engineering and Geosciences, Polytechnic University of Catalonia (UPC), Spain
[b] Institute of Geotechnical Engineering, RWTH Aachen University, Germany
[c] School of Science and Engineering, University of Dundee, UK

Received 25 August 2020; received in revised form 24 January 2021; accepted 5 March 2021
Available online 5 April 2021

Abstract

Sand roughness is now accessible to measurement. Incorporating this parameter into sand models using the discrete element method (DEM) is known to improve bulk small strain response. In this work we explore the effect on problems where particle crushing takes place. A well-established DEM particle crushing model and a rough Hertzian contact model are here combined to incorporate both effects in a single contact model. Including contact roughness results in stronger particles whilst all other material parameters being equal. The model is then used to simulate high pressure oedometric compression tests on a strong silica sand. It is shown that including realistic values of surface roughness enables to correctly capture both load-unload behaviour and particle size distribution evolution while using realistic values of elastic bulk properties for the sand grains. Roughness is then a model refinement that may result in simpler, more objective DEM calibrations.

Keywords: Surface roughness; Discrete-element modelling; Particle crushing/crushability; Stress path; Stress analysis

1. Introduction

The discrete element method (DEM) is widely applied for modelling granular materials. In soil mechanics DEM is now systematically used at specimen scale to explore in detail many fundamental aspects of soil behaviour, like particle crushing (Hanley et al., 2015), interface effects (Zhang and Evans, 2018), fabric effect on liquefaction (Wang et al., 2016), debonding (Shen et al., 2019), etc. DEM is also increasingly used to analyze large scale problems of direct engineering relevance (Ciantia et al., 2016; Zhang et al., 2019; Garcia and Bray, 2018; Butlanska et al., 2018; Kawano et al., 2018; Ciantia et al., 2019a; Zhang et al., 2021). A singular advantage of DEM models is their potential to incorporate grain scale information in the formulation of element behaviour and/or element interactions. This feature may lead to greatly simplified model calibration, bypassing the perennial soil mechanics problem of obtaining and testing representative samples. Within this perspective, the question is then to identify and incorporate into discrete models measurable grain scale features of geotechnical significance, like grain strength (Ciantia et al., 2015) or grain shape.

When considering grain shape, a scale-based separation of relevant descriptors is frequently used. Barret (1980) defined shape as the combination of three aspects: form, measured at particle scale, roundness, measured at an intermediate scale, and surface texture, measured at small scale. A large amount of work has been devoted to represent grain shape features in DEM models, but most of it has focused on the larger scale features that correspond to form and roundness (Coetzee, 2016; Rorato et al., 2021) and far less attention has been paid to roughness.

Peer review under responsibility of The Japanese Geotechnical Society.
* Corresponding author.
E-mail address: m.o.ciantia@dundee.ac.uk (M.O. Ciantia).

https://doi.org/10.1016/j.sandf.2021.03.002

Nomenclature

A_F	contact area between particles
C_v	coefficient of variation
d	particle size
d_0	reference size of sphere
d_{50}	median d
d_{av}	average particle diameter
d_c	comminution limit
d_{max}	maximum d assumed for the limit distribution
d_{min}	minimum d assumed for the limit distribution
e	void ratio
E_1, E_2	Young's modulus of particle
F_1	contact force in asperity-dominated regime
F_2	contact force in transition regime
F_3	contact force in Hertzian regime
F_{lim}	limit contact force
$F_{lim,av}$	average limit contact force
F_n	normal contact force
F_{nT1}, F_{nT2}	threshold normal inter-particle contact force
$f(var)$	effect of variability of particle strength
G	shear modulus
I_G	grading state index
k_n	normal contact stiffness
k_s	shear contact stiffness
$L(Fn)$	limit breakage condition
$L_A(Fn)$	$L(Fn)$ in asperity-dominated regime
$L_T(Fn)$	$L(Fn)$ in transition regime
$L_H(Fn)$	$L(Fn)$ in Hertzian regime
$M_{(L<d)}$	mass of particles smaller than d
M_T	total mass of sample
N°	particle numbers
n_1, n_2	coefficients
p'	mean effective pressure
q	deviatoric pressure
r_1, r_2	radius of contacting spheres
r_H	radius of contact area
S_q	particle surface roughness
var	coefficient of variation
v_1, v_2	Poisson's ratios
$X_{0,1}$	random number sampled from standard normal distribution
Z^m	mechanical coordination number
ε_z	axial strain
ε_{vol}	volumetric strain
σ'	effective confining pressure
σ_{lim}	limit strength of material
$\bar{\sigma}_{\lim}$	mean strength for a sphere of diameter d
$\sigma_{lim,0}$	$\bar{\sigma}_{\lim}$ for a sphere at the reference size d_0
σ_{SD}	normally distributed limit strength of material
σ_z	vertical stress
δ	contact overlap
δ_1, δ_2	dimensional constants
δ_{T1}, δ_{T2}	threshold contact displacements
α	fractal dimension of the limit grading
μ	coefficient of inter-particle friction
η	q/p′, pressure obliquity

Experiments show, however, that particle roughness, by itself, strongly modifies basic engineering properties of granular materials, like stiffness, frictional strength or limiting densities. Those effects have been unequivocally identified through careful testing of simple granular materials like steel balls or glass beads (Santamarina and Cascante, 1998; Sharifipour and Dano, 2006; Cavaretta et al., 2010; Otsubo et al., 2015; Otsubo and O'Sullivan, 2018).

Considering natural sands the situation is more complex. Particle surface roughness can be now accurately characterized and quantified, most typically using optical interferometry (Table 1). Nardelli and Coop (2019) demonstrated that particle roughness does have a major effect on interparticle contact properties, such as friction and stiffness. However, it is difficult to experimentally isolate the effects of grain roughness on macroscopic behavior, separating them from those of larger scale shape features. On the other hand, such experimental difficulties can be overcome when using the discrete element method, as it allows to switch on and off different microscale features.

It appears then that incorporating particle surface roughness may be important for discrete models of granular materials. This is done advantageously through modification of the contact model, and several proposals have been presented to investigate that effect (Cavarretta et al., 2010; Otsubo et al., 2017a; Zhao et al., 2018; Nadimi et al., 2019). The benefits of that approach were clear in the work of Otsubo and O'Sullivan (2018), who showed that the model by Otsubo et al. (2017a) was able to capture well the experimental pressure-dependency of small-strain stiffness in glass beads.

Including roughness in the contact model has implications for other aspects of discrete soil models. All the rough contact models mentioned above take Hertzian smooth contact theory as a starting point. In that theory the elastic properties of the material forming the grains, i.e. shear modulus, G, and Poisson ratio, υ, control contact stiffness. In principle, this should be beneficial for DEM calibration, as elastic properties for many basic minerals are well known. For instance, tabulated G values for quartz range from 27.9 GPa to 32.3 GPa (see https://www.azom.com/properties.aspx?ArticleID = 1114). In practice, much smaller G values than those of the mineral are frequently calibrated when DEM is used to reproduce experimental

Table 1
Experimentally measured roughness statistics.

Source	Sand	Method	N°	d_{av}/mm	Mean roughness /μm	Roughness range/μm	Stdv/μm
Alshibli and Alsaleh (2004)	F sand (Ottawa F-75)	Optical interferometry	120	0.22	0.98	0.31–3.1	0.61
Alshibli and Alsaleh (2004)	M sand	Optical interferometry	120	0.55	1.08	0.39–3.1	0.66
Alshibli and Alsaleh (2004)	C sand	Optical interferometry	120	1.6	1.23	0.77–2.9	0.52
Cavarretta et al. (2010)	LBS	Optical interferometry	10	1.5	0.3	–	–
Senetakis et al (2013)	LBS	Optical interferometry	50	2.36	0.38	–	0.19
Nardelli and Coop (2019)	LBS	Optical interferometry	20–30	2.36	0.29	–	–
Yao et al (2018)	LBS	Optical interferometry	50	2	0.42	0.34–0.55	0.054

behaviour (Xu et al., 2015; Salazar et al., 2015; Irazábal et al., 2017). Lower G values have the advantage of reducing the computational cost, as larger timesteps may be employed in simulation (Otsubo et al., 2017b). However, by calibrating particle moduli on macroscale responses, the physical meaning of the parameters becomes obscure. Harkness et al (2016), working with ballast, noted that low G values also achieved better match with experimental responses for monotonic loading, but the opposite was true for load –unload cycles. They went on to modify the Hertzian contact model to represent asperity crushing – a feature with close similarity to roughness- and solved this apparent contradiction.

This difficulty in selecting appropriate values of particle elastic stiffness is increased when particle breakage is also modelled. Particle breakage plays a fundamental role in some important geotechnical applications, e.g. pile shaft friction (Tamura et al., 2012; Yang et al., 2014). Although other methods may be applied, DEM studies of particle breakage gain predictive power if based on the particle replacement method (Lobo-Guerrero and Vallejo, 2005; Ciantia et al., 2015; Hanley et al., 2015).

When using the particle replacement method and Hertzian contact there is, again, disagreement on the values of G to use. Some researchers (Ciantia et al., 2015, Chaudry et al., 2018; Liu et al., 2019; Wang et al., 2019, Ciantia and O'Sullivan, 2020) use values that are way below experimental material values. Others (Hanley et al., 2015; de Bono and McDowell, 2018; Zhou et al., 2020) use realistic material values. Part of the motivation for using low G values is related to computability: particle replacement quickly increases the number of particles in simulation and increasing the time step may compensate for it. The alternative is to use a large computer – as done by Hanley et al. (2015) or Zhou et al. (2020)- or to reduce the number of initial particles in simulation –the case of De Bono and McDowell (2014). But there are also more fundamental reasons to use a reduced stiffness value. These are linked to the effect that contact stiffness has on particle breakage: high contact stiffness typically increases particle breakage, affecting mechanical responses and grain size evolution.

A possible way out of these difficulties is explored here. It is hypothesized that, by incorporating roughness in a contact model description, the use of more realistic values of contact stiffness is possible, without losing the ability to obtain a good reproduction of high stress phenomena dominated by breakage. Although the link between crushing and large-scale particle shape features -form, roundness- has been explored before using DEM models (Fu et al., 2017; Ma et al., 2019) this is not the case for the connection between roughness and crushability, which is the focus of this work.

In the following sections we first describe how a contact model including particle surface roughness for crushable particles is established. Contact model parameters are then recalibrated for a discrete analogue of a representative quartz sand and some simulation results obtained to validate the new model are presented and discussed.

2. Contact model for rough crushable particles

2.1. Model description: roughness effect on normal contact

For a standard Hertzian contact model, the normal force-displacement relationship for a smooth contact between two spheres is given as (Thornton, 2015)

$$F_n = \frac{4}{3}E'\sqrt{r'}\delta^{1.5} \tag{1}$$

where, F_n is the normal contact force, δ is the contact overlap and E' and r′ are given by

$$E' = \left(\frac{1-v_1^2}{E_1} + \frac{1-v_2^2}{E_2}\right)^{-1} \tag{2}$$

$$r' = \left(\frac{1}{r_1} + \frac{1}{r_2}\right)^{-1} \tag{3}$$

The subscripts '1′ and '2′ refer to the two contacting particles. E_i, v_i and r_i are the Young's modulus, the Poisson's ratio and the radius of particle i, respectively. Inspired by Greenwood and Tripp (1967), Otsubo et al. (2017a) generalized the Hertzian model proposing a three-stage F_n-δ relationship for rough contact (Fig. 1). In the Otsubo et al. (2017a) formulation when

$$F_n < F_{nT1} = S_q E'\sqrt{2r'S_q} \tag{4}$$

asperities, characterized by the roughness parameter S_q, dominate the F_n-δ relationship and the contact is more compliant than when

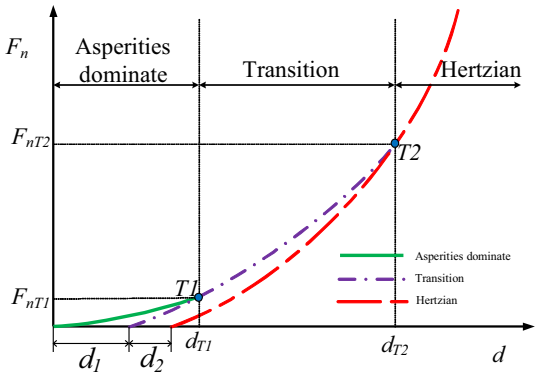

Fig. 1. Schematic illustration of rough surface contact model (Otsubo et al., 2017a).

$$F_n > F_{nT2} = 100F_{nT1} \tag{5}$$

which is the threshold force above which the contact starts to behave in agreement with the standard Hertzian model. The ratio 100 between F_{nT2} and F_{nT1} originates from experiments on rough hard materials (Greenwood and Tripp, 1967; Cavarretta et al., 2010).

Thus, the F_n-δ relationship is thus described by three expressions, corresponding to three successive contact regimes: asperity-dominated, Eq. (6), transitional, Eq. (7) and Hertzian, Eq. (8).

$$F_n = F_{nT1}\left(\frac{\delta}{\delta_{T1}}\right)^c \qquad \delta \leqslant \delta_{T1} \tag{6}$$

$$F_n = F_{nT2}\left(\frac{\delta - \delta_1}{\delta_{T2} - \delta_1}\right)^b \qquad \delta_{T1} < \delta < \delta_{T2} \tag{7}$$

$$F_n = \frac{4}{3}E'\sqrt{r'}(\delta - \delta_1 - \delta_2)^{1.5} \qquad \delta_{T2} \leqslant \delta \tag{8}$$

δ_{T1} and δ_{T2} are threshold contact displacements that correspond to contact forces equal to F_{nT1} and F_{nT2} respectively. b and c are constants that ensure slope continuity for the overall F_n-δ relation and depend only on two model parameters δ_1 and δ_2. As shown in Fig. 1, the values of δ_1 and δ_2 would correspond to contact displacements obtained if unloading from the transitional and Hertzian regime, respectively. However, following Otsubo et al. (2017a), no separate unloading branches are employed in the model and a single loading–unloading curve, with no residual displacement, is used instead. The values of δ_1 and δ_2 are both function of S_q and are expressed as:

$$\delta_1 = n_1 S_q \tag{9}$$

and

$$\delta_2 = n_2 S_q \tag{10}$$

where n_1 and n_2 are model parameters. These model parameters might be calibrated against the results of single grain contact force–displacement experiments. When $S_q = 0$, the standard Hertzian theory is recovered.

In the model, particle surface roughness is represented by the parameter S_q. Roughness generally refers to asperities at the surface of granular materials such as sands, which can be precisely quantified through different laboratory procedures, although for sand particles optical interferometry is most often employed (Yao et al., 2018). A variety of surface roughness parameters result from such measurements. Two often used in soil mechanics oriented testing (Altuhafi et al., 2016) are S_q, which is the root mean square of the elevations of data points relative to a reference surface i.e:

$$S_q = \sqrt{\frac{1}{n}\sum_{i=1}^{n}\left(Z_i^2\right)} \tag{11}$$

and S_a, which is the mean of the absolute values of the elevations from a reference surface:

$$S_a = \frac{1}{n}\sum_{i=1}^{n}|Z_i| \tag{12}$$

Each of these measures has certain statistical significance, for instance S_q has the format of a standard deviation, while S_a is a mean deviation. The inherent analytical advantages of standard deviation may explain why most recent work is based on S_q (Otsubo et al., 2015; Yao et al., 2018). Regardless of the definition adopted, the experimental contact behavior will not change. There would always be an asperity dominated region, a transition zone and finally region not affected by roughness. This is what the model represents and is independent of the particular procedure employed to measure roughness.

The effect of roughness that is incorporated in the model does only affect contact stiffness. Although there is also some recent evidence on roughness effects on inter-particle friction for sands (Nardelli and Coop, 2019) this aspect was left aside in the current work. Therefore, the friction coefficient is considered to be roughness-independent in the model.

2.2. Model description: roughness effect on crushing limit

Particle crushing imposes a limit to the contact normal force acting on a particle. Following Ciantia et al. (2015) such limit can be expressed as:

$$F_n \leqslant \sigma_{\lim} A_F \tag{13}$$

where σ_{lim} is the limit strength of the particle and A_F is the contact area. As detailed in Ciantia et al. (2015) the expression above follows from work of Russell et al. (2009) based, in turn, on a bi-parametric strength criteria (Christensen, 2000); as such, the limit strength σ_{lim} is different from the uniform tensile stress that is frequently used to interpret particle crushing experiments (Nakata et al. 1999). Expressing the failure criteria in this way allows

for a clear separation of the effects of particle strength (σ_{lim}) and contact area, (A_F).

- Particle strength, σ_{lim}:

A stochastic model of particle strength is employed. For fixed particle diameter the limit strength is normally distributed with mean value given by $\bar{\sigma}_{lim}$ and standard deviation given by $\sigma_{SD} = var\,\bar{\sigma}_{lim}$. The coefficient of variation of these distributions, '*var*', is a material parameter and is assumed independent of particle size. On the other hand, to take into account that smaller particles are stronger, the mean value $\bar{\sigma}_{lim}$ is size-dependent. Size effects on particle strength are formulated following McDowell et al. (2013),

$$\bar{\sigma}_{\lim} = \sigma_{\lim,0}\left(\frac{d}{d_0}\right)^{-3/m} \tag{14}$$

where, m is a material parameter and $\sigma_{lim,0}$ is the mean value of the limit strength at the reference diameter d_0 (in this work chosen as 2 mm). In the simulation the limit strength value for any particle, σ_{lim} is initialized sampling from the normal distribution that corresponds to its size. The full expression is

$$\sigma_{\lim} = \bar{\sigma}_{\lim} f(\mathrm{var}) = \bar{\sigma}_{\lim}(1 + var\mathrm{X}_{0,1}) \tag{15}$$

where, $X_{0,1}$ is a random number sampled from the standard normal distribution.

- Contact area, A_F:

The expression for contact area A_F is given by Otsubo et al. (2017a) as:

$$A_F = \pi r_H^2 = \pi r' \delta \tag{16}$$

Where r_H is the radius of contact area between particles and the contact overlap, δ, can be obtained from Eqs. (6)–(8). Contact stiffness will affect the way A_F evolves with F_n since, for a given contact force, the contact area will be larger or smaller depending on the particle stiffness (slope of the F_n-δ curve).

As shown in the Appendix, combining the normal force vs normal displacement expressions of the rough contact model (Eqs. (6)-(8)) with the particle failure criterion expressed by Eqs. (13)–(16) it is possible to obtain three different equations for the limiting breakage condition, $L(F_n)$ one appropriate to each contact regime. In the asperity-dominated regime, when $F_n < F_{nT1}$

$$L_A(F_n) = F_n - \sigma_{\lim}\pi r'\left(\frac{F_n}{S_q E'\sqrt{2r'S_q}}\right)^{\frac{1}{c}} \left\{\left(\frac{1}{100}\right)^{\frac{1}{b}}\left[\left(\frac{300S_qE'\sqrt{2r'S_q}}{4E'\sqrt{r'}}\right)^{\frac{2}{3}} + n_2S_q\right] + n_1S_q\right\} \leqslant 0 \tag{17}$$

in the transitional regime, when $F_{nT1} \leq F_n < F_{nT2}$

$$L_T(F_n) = F_n - \sigma_{\lim}\pi r' \left\{\left(\frac{F_n}{100S_qE'\sqrt{2r'S_q}}\right)^{\frac{1}{b}}\left[\left(\frac{300S_qE'\sqrt{2r'S_q}}{4E'\sqrt{r'}}\right)^{\frac{2}{3}} + n_2S_q\right] + n_1S_q\right\} \leqslant 0 \tag{18}$$

and in the Hertzian regime, when $F_{nT2} \leq F_n$

$$L_H(F_n) = F_n - \sigma_{lim}\pi r'\left[\left(\frac{9F_n^2}{16E'^2r'}\right)^{\frac{1}{3}} + n_1S_q + n_2S_q\right] \leq 0 \tag{19}$$

These limiting breakage conditions, which are implicit on the normal force, are explored later. For the moment is worth noting that as the value of roughness S_q tends to zero so do F_{nT1} and F_{nT2}, i.e. the force values that mark the boundary between the different contact regimes. The only surviving limiting condition is then that of the Hertzian regime, L_H, which, when $S_q = 0$ reduces to that used in the smooth contact model.

Other aspects of the particle breakage model remain identical to those presented by Ciantia et al. (2015). Once a limit condition is reached, a particle is replaced by 14 smaller inscribed tangent spheres. This 14-sphere configuration was adopted balancing two fundamental computational aspects: accuracy and cost. The spawned fragments inherit the velocity and material parameters of the original particle apart from the intrinsic strength σ_{lim} that is randomly sampled from the corresponding size distribution. A fraction of the broken particle volume is lost upon breakage; it is assumed that the material lost corresponds to fines that are accounted for in the determination of the material grading. This is a highly simplified representation of breakage events, justified because network induced effects of breakage are far more important (Wang and Arson, 2018) and are well captured by the model (Ciantia et al., 2019b).

As the number of fragments spawned in a breakage event increases, the amount of volume lost at each breakage reduces, but the computational cost increases. A numerically motivated comminution limit, d_c, is imposed to stop crushing of smaller particles. The grading state index I_G, introduced by Muir Wood (2007) to quantify grading by means of a scalar quantity (Fig. 2), is computed as the area ratio of the current grading to a limit grading. The limit grading is given by a fractal distribution with a fractal dimension $\alpha = 2.6$; this distribution can be expressed as (Einav, 2007)

$$\frac{M_{(L<d)}}{M_T} = \frac{d^{3-\alpha} - d_{\min}^{3-\alpha}}{d_{\max}^{3-\alpha} - d_{\min}^{3-\alpha}} \tag{20}$$

where, M_T is the total mass of the sample, $M_{(L<d)}$ is the mass of particles smaller than d, d_{max} and d_{min} are, respectively, the maximum and minimum particle sizes assumed for the limit distribution. The same limit distribution formula, but now with d_{max} given by the smallest particle created during the crushing event, is used during post-

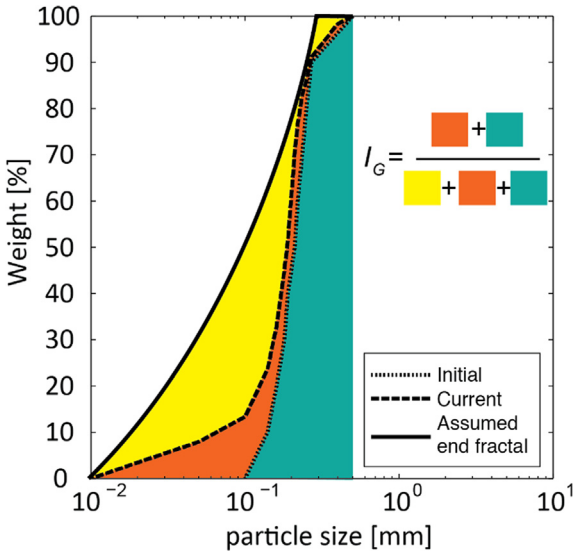

Fig. 2. Grading index I_G definition (Muir Wood, 2007).

processing to assign a size distribution to the volume lost at each crushing event.

2.3. Numerical implementation

The newly proposed contact model for rough particles was implemented in the commercial code PFC3D V5 (Itasca, 2017) by means of a C++ coded user defined contact model (UDCM). When roughness is not present the UCDM includes as a subset the breakable particle model, which in previous work (Ciantia et al., 2015) had been implemented using higher level FISH-language algorithms. The main difference between the FISH and UDCM implementations is that a time-consuming loop through all the contacts is required in the FISH implementation, but not in the UDCM. In fact, in PFC5, during the execution of force–displacement law, there is a loop over all the contacts, regardless of the type of selected contact model. During one step, the UDCM collects the information of particles that meet the crushing criterion into a signal. The signal is then emitted to call another FISH function that performs the 14-ball replacement for these particles. Using the smooth contact model, Ciantia et al. (2017) discussed the computational efficiency gains derived from using the UDCM to detect particle breakage.

2.4. Validation

To validate the correct implementation of the rough contact crushable model, the analytical expressions for ball-ball contact and ball-wall contact forces were independently evaluated for some elementary configurations and the results compared with those obtained from the UDCM. The results obtained are illustrated in Fig. 3 and the parameters adopted for this check are listed in Table 2. Two tests are considered: the compression of two identical spheres and the compression of a sphere between two rigid walls. In the figure F_1, F_2 and F_3 represent contact forces in asperity-dominated (purple thick line), transition (blue medium thick line) and Hertzian (green thin line) regimes, respectively. The black dotted line F_{lim} indicates the analytical limit crushing force, while the black square marks the 'failure' point of the UDCM response (red line). The good agreement between the analytical curves and the UDCM validates the numerical implementation of the contact model. The dotted line labelled $S_q = 0$, corresponding to a Hertzian smooth contact model with crushing inhibited, is included for reference. As expected, the rough contact model results in larger contact overlap than the smooth model. The difference increases with the value of F_n.

3. Effect of contact roughness on single particle breakage

Introduction of roughness does not only result in a modified normal contact stiffness. Through their effect on contact area, the three new parameters (i.e. surface roughness S_q, and coefficients n_1 and n_2) modify the onset of particle breakage as evidenced by the different limiting breakage

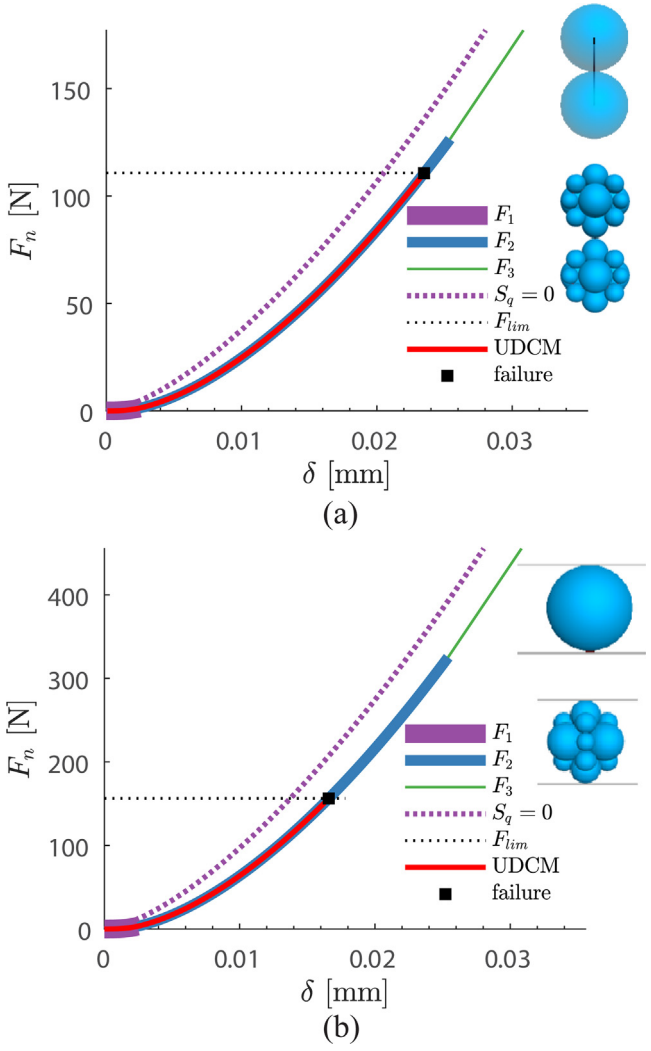

Fig. 3. Validation of the PFC3D implementation of the contact model (UDCM): (a) ball-ball contact, (b) ball-wall contact.

Table 2
Parameters for UDCM validation.

Parameters	d/mm	G/GPa	v	μ	m	$\sigma_{lim,0}$/GPa	S_q/μm	n_1	n_2
Values	2	32	0.2	0.275	7.5	3	1.0	1	2

conditions $L(F_n)$ (Eqs. (17)-(19)) that apply in the different contact regimes. A series of parametric analyses were performed to investigate this coupling.

In the first suite of parametric analyses, PFC3D is used to simulate crushing of a silica sand grain between flat steel platens, a classical experimental configuration for this kind of study (Nakata et al., 1999). To do so the moduli of silica (E_1 = 76.8 GPa, v_1 = 0.2) and steel (E_2 = 768 GPa, v_2 = 0.2) are used in Eq. (2) and, according to Eq. (3), $r' = r_1$ in Eqs. (17)–(19). The simulations are followed up until the moment of first particle breakage, as the model does not intend to represent post-peak particle failure behaviour.

The reference parameter set used for this study is reported in Table 2. This parameter set is referred to by the shorthand 'Base' in Table 3, where other variant parameter sets are listed. The solid thick line illustrated in each subplot of Fig. 4 represents the result of the reference parameter set. Increasing either roughness (S_q) or the n_i ratios results in less stiff contact behaviour and increased forces at failure. Larger forces are required to crush rough particles, since, for a given force, a more compliant contact results in larger particle overlaps and contact areas.

Table 3
Parameter variants for parametric study of single particle crushing test (Fig. 4).

Tests	S_q/μm	n_1	n_2
Base	1.0	1.0	2.0
S_q_0.0	0.0	1.0	2.0
S_q_2.0	2.0	1.0	2.0
S_q_3.0	3.0	1.0	2.0
n_1_0.0	1.0	0.0	2.0
n_1_0.5	1.0	0.5	2.0
n_1_2.0	1.0	2.0	2.0
n_2_0.0	1.0	1.0	0.0
n_2_0.5	1.0	1.0	0.5
n_2_2.0	1.0	1.0	2.0

A second parametric study (Fig. 5) explores the effects of a larger range of S_q, n_1 and n_2 on the limiting crushing force. For each parameter combination Fig. 5 represents several relevant results, namely

1. The values of forces F_{NT1} and F_{NT2} that mark the boundaries between the asperity dominated, transitional and Hertzian contact regimes.
2. The three limiting breakage conditions for the different contact regimes, that is $L_A(F_n)$, $L_T(F_n)$ and $L_H(F_n)$ as given by Eqs. (17)–(19). The implicit equations, evaluated using the MATLAB solver 'fsolve', are plotted for all F_n values, even those beyond the contact regime in which they apply.
3. The actual limiting breakage condition, $L(F_n)$, which is an envelope that results from joining $L_A(F_n)$, $L_T(F_n)$ and $L_H(F_n)$ when these are restricted to the F_n values of the regime in which they apply.

As a visual aid, in Fig. 5 the parameter domain corresponding to each contact regime is shaded by a different colour. Also, the $L(F_n)$ value corresponding to the reference set is marked ("base").

The figures reflect how the frontiers between different particle crushing regimes depend only on roughness but not on parameters n_1 and n_2. Generally speaking, the effect of those two parameters is relatively modest, not affecting significantly the crushing contact force until they reach rather high values – i.e. values above 1 that would imply

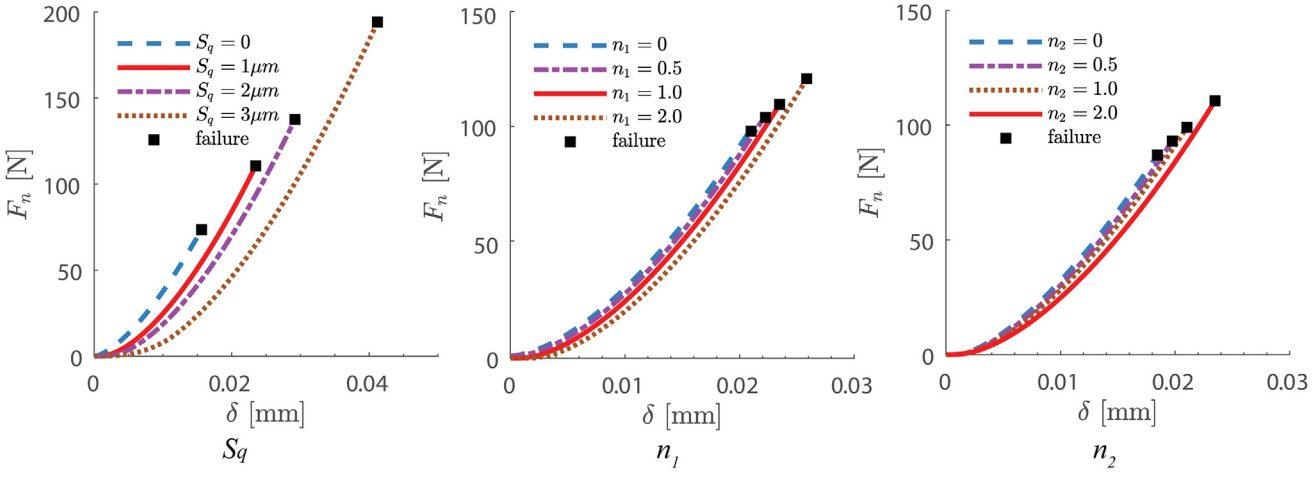

Fig. 4. Parametric study over three new parameters (S_q, n_1, and n_2) in the crushing model.

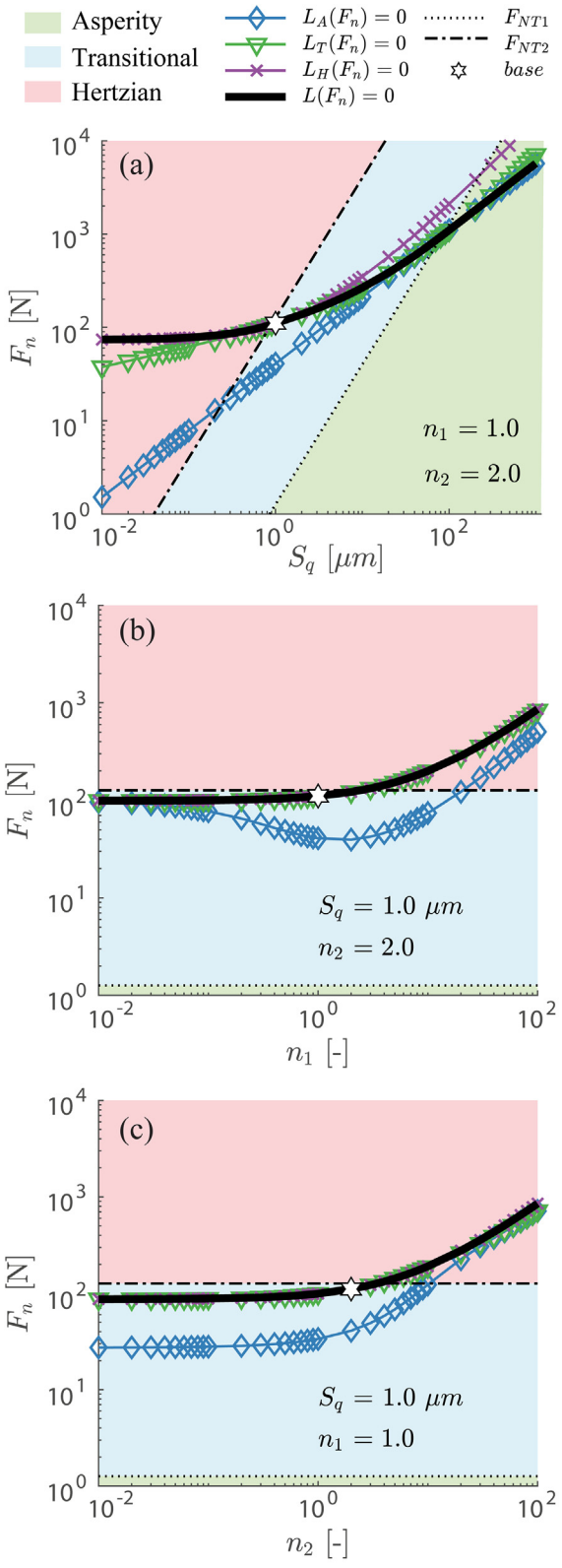

Fig. 5. Parametric study over wide ranges of the new variables (S_q, n_1, and n_2). Other parameters as in the base parameter set in Table 3.

residual normal displacements (δ_1, δ_2) much larger than roughness itself. The effect of roughness S_q is more significant. The results indicate that for relatively small roughness values, (say for $S_q < 0.1$ μm), the limiting breakage condition, $L(F_n)$, is independent of roughness and failure takes place in the Hertzian regime. As roughness increases, the limiting breakage condition also increases and failure takes place in the transition regime or even (for $S_q > 20$ μm) in the asperity-dominated contact regime.

In Fig. 5a roughness was varied while maintaining a constant particle diameter of 2 mm, -at the upper limit of what may be conventionally described as sand (ISO 17689-1, 2017).

It is interesting to explore the effect of varying particle diameter while maintaining roughness constant. That is done in Fig. 6 for a particle diameter range that goes from fine sands (0.1 mm) to medium gravels (10 mm), with

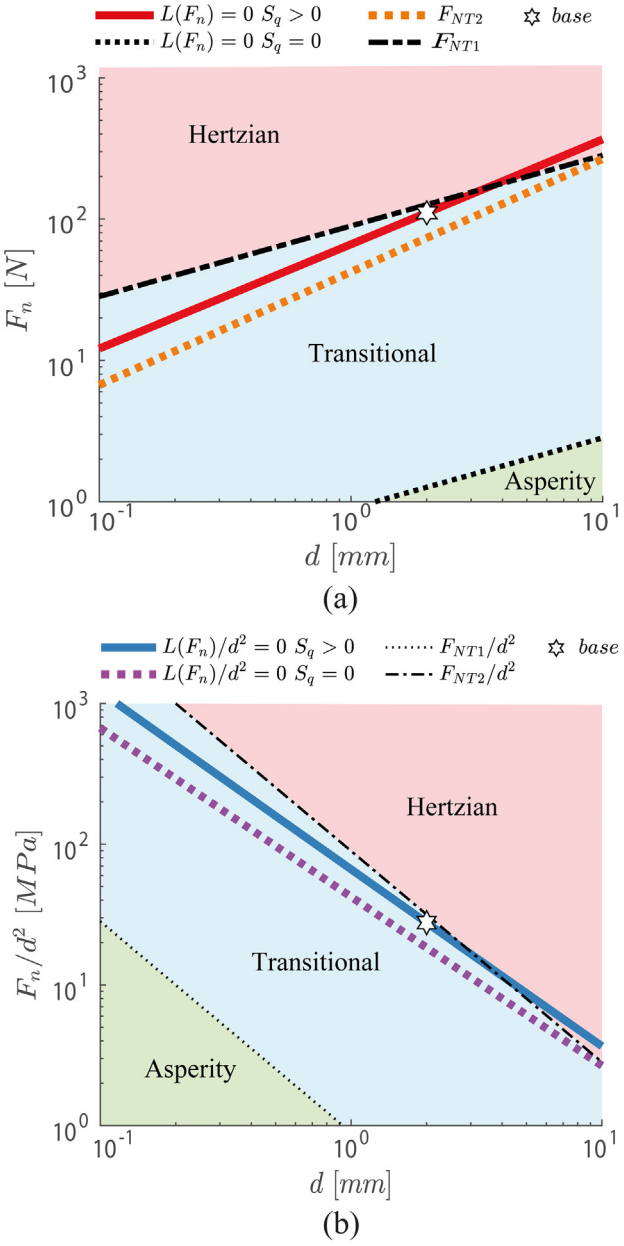

Fig. 6. Effect of particle size within the rough contact model on (a) particle breakage force (b) nominal tensile strength. Model evaluated for the base parameter set in Table 3.

roughness kept constant at 1 μm. For comparison purposes, a smooth case with zero roughness is also evaluated. Other parameters are maintained as in the base case in Table 2.

Fig. 6 shows that, affected by the inclusion of roughness, the limiting force (Fig. 6a) and nominal strength (Fig. 6b) increase, and that effect is nearly independent of particle size. Therefore, the curves with roughness ($S_q > 0$) are simply an upward translation of the curves without roughness ($S_q = 0$). The failure of larger particles starts to take place above the Hertzian contact limit.

4. Effect of contact roughness on sand high stress behaviour

4.1. Limitations of the smooth crushable model

To evaluate the effect of roughness in specimen scale response, this section re-examines some results presented in a recent study by Ciantia et al. (2019c). That study describes the effect of grain crushing on the position of critical state line of a silica sand, Fontainebleau sand. DEM simulations were performed using the crushable particle model described above, but always using a smooth Hertzian contact.

As detailed in Ciantia et al. (2019c) the model parameters for the sand were calibrated and validated by reproducing a variety of tests, including single particle crushing tests and specimen-scale tests. These included a series of oedometers on identically prepared specimens that were subject to different maximum applied vertical stresses (25 MPa, 50 MPa, 75 MPa and 100 MPa). After dismounting each experiment the final grading index I_g was measured, thus obtaining a grading evolution path.

In DEM, the oedometer tests are simulated using a 4 mm sided cube of frictionless rigid walls filled with 10,000 spherical particles. Particle diameter ranged from 0.1 to 0.4 mm matching the PSD of Fontainebleau NE34 sand. The target void ratio before loading was attained as 0.64. The vertical stress during the simulations adopted the same logarithmic control of the load increment proposed by Ciantia et al. (2015). The parameters calibrated in Ciantia et al. (2019c) are recalled in Table 4 -identified with the label 'low G'. The simulated oedometer results – loading-unloading response and I_G evolution- using these parameters are presented in (Fig. 7a, b).

The DEM smooth crushing model was successful in reproducing the loading and grading evolution curves, however the unloading paths showed far too much elastic rebound. The work of Harkness et al. (2016) suggests that this mismatch on unloading was likely due to the low G employed (a value $G = 9$ GPa was input). This low G value has also the inconvenient of being very different from those expected for quartz.

In (Fig. 7c, d) the same tests are simulated again with the smooth crushable model, but now using a higher -although realistic for quartz-G value of 29 GPa ('high G' set in Table 4). The loading-unloading curve match with the experimental data is much improved, however, a clear discrepancy is now apparent non the I_G tracking curve especially in the low-pressure regime. The increase of contact stiffness causes excessive and fast development of crushing events. This may be avoided if surface roughness is included in the model, as shown in the next section.

4.2. Application of the rough crushable model

The rough contact crushable model adds three new parameters (S_q, n_1 and n_2) to the 'old' model parameters (G, v, μ, var, m and $\sigma_{lim,0}$). Broadly speaking, G, v, μ, S_q, n_1 and n_2 are contact parameters while var, m and $\sigma_{lim,0}$ define particle strength. Wishing to use realistic, material-based values, G was assigned a value of 32 GPa and v a value of 0.19, as appropriate values for SiO_2 according to an industrial database. Particle interface friction coefficient μ has the same value as that in the previous work (Ciantia et al., 2019c). The remaining parameters (S_q, n_1, n_2, $\sigma_{lim,0}$, var and m) are calibrated in a two steps:

1. S_q is set as 0.6 μm, considered as a realistic roughness value for silica sand (Table 1). The values of n_1 and n_2 were set as 0.05 and 5, respectively after calibration against the results of contact experiments on LBS fraction A reported by Nardelli and Coop (2019). The calibration is shown in Fig. 8.
2. Experimental data on size dependency of flat-platen single particle crushing forces indicates the value of m (Fig. 9a). As already noted by Ciantia et al. (2019c) the strength size effect calibrated with this model (embedded in the m value) seems far smaller than what had been previously thought (Fig. 9b). This dataset also indicates a likely range for $\sigma_{lim,0}$. var is calibrated fitting a normal distribution to particle size strength variability as described in (Ciantia et al., 2019c).

Experimental data from the literature of single particle crushing test where values of both F_{lim} and S_q values were measured is reported in Table 5. In cases where both F_{lim}

Table 4
Calibrated parameters for Fontainebleau sand.

	G/GPa	v	μ	m	$\sigma_{lim,0}$/GPa	var	d_c/d_{50}	d_{max}/mm	d_{min}/mm	S_q/μm	n_1	n_2
Smooth crushable model- low G	9	0.2	0.275	10	1.9	0.36	0.55	0.27	0.01	–	–	–
Smooth crushable model-high G	29	0.2	0.275	10	6	0.36	0.55	0.27	0.01	–	–	–
Rough-crushable model	**32**	**0.19**	0.275	**12**	**3.75**	**0.38**	0.55	0.27	0.01	**0.6**	**0.05**	**5**

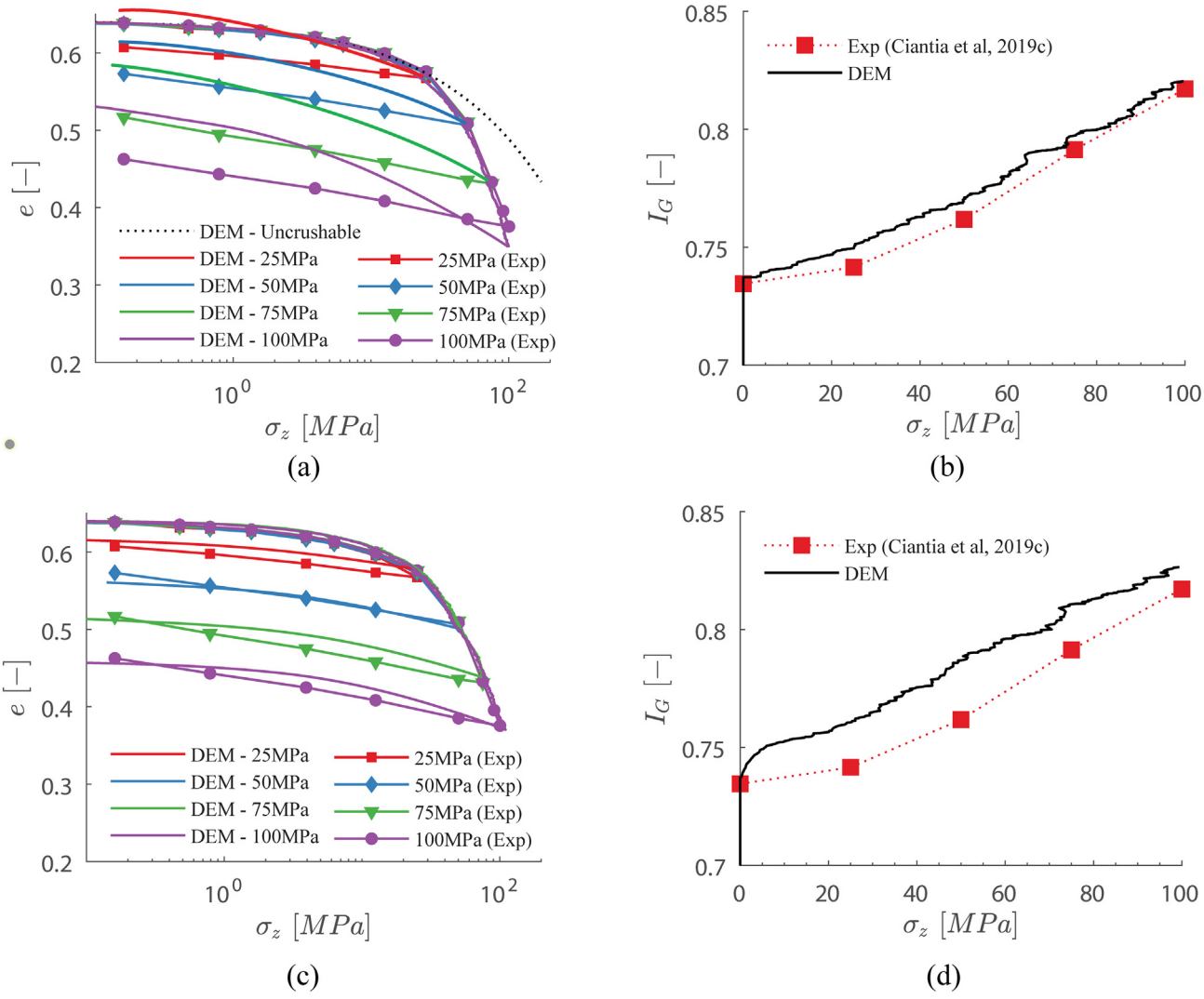

Fig. 7. Effect of particle stiffness in a crushable DEM model of Fontainebleau without roughness: (a), (b) $G = 9$ GPa and (c), (d) $G = 29$ GPa.

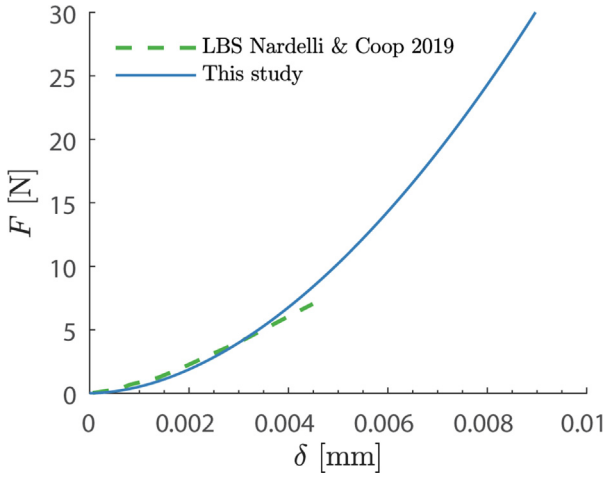

Fig. 8. Load displacement relationship of single grain test.

and S_q were not available in the same paper, combined results from multiple sources on the same sand are reported. Fig. 10 compares our calibrated crushing model for particles of $d = 1.75$ mm with the experimental values in Table 5 of particles with diameters in the range of our theoretical curve (1.5 mm $< d <$ 2 mm). According to our model definition, Fig. 10 suggests that crushing of silica sand grains of this size range mostly happens in the Hertzian contact regime. This result is reasonable as silica sand is known to be a relatively strong sand, able to sustain the high loads necessary to reach the Hertzian regime.

With this estimation of parameters (Table 4), the DEM model for rough crushable particles is run to simulate the oedometric compression curve (both loading and unloading). The results are quite satisfactory (Fig. 11). Clearly, the loading curve and grading evolution are as good as those obtained using the smooth model with a low G value

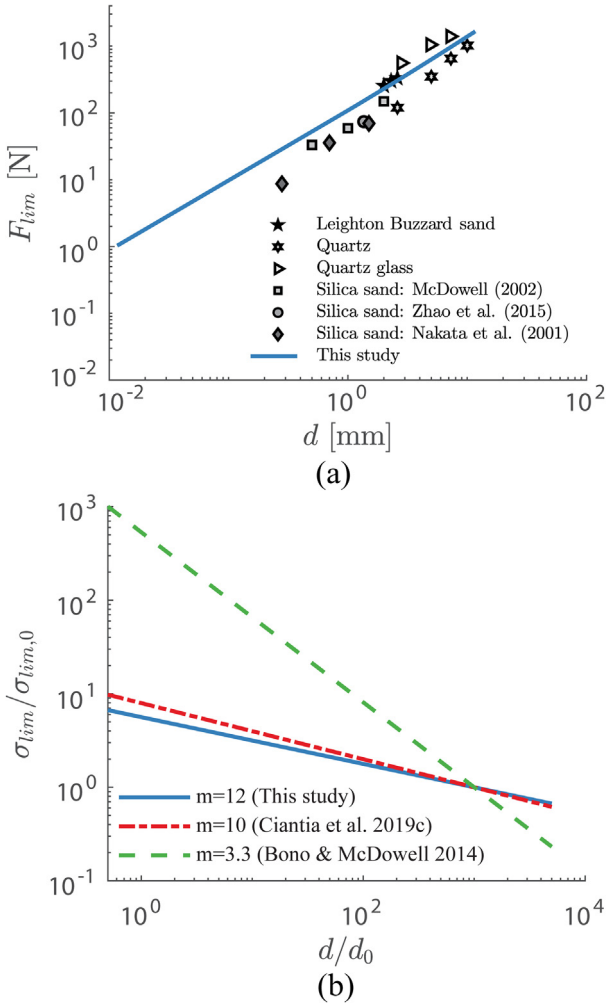

Fig. 9. (a) Calibration of crushing-related parameters of the contact model using flat-platen single-particle crushing test data. (B) effect of roughness on 'size effects'.(See above-mentioned references for further information.)

(Fig. 7a, b). The unloading curve is now captured almost as well as with the smooth model with the high G value (Fig. 7c).

4.3. Further validation of the model

A further validation of the model was attempted. Luong and Touati (1983) reported a series of high-pressure isotropic (σ_r = 0.5, 6, 16 and 30 MPa) and triaxial compression tests on dense Fontainebleau sand. These tests were already reproduced by Ciantia et al. (2019c) using the 'low-G' parameter set with the smooth model.

Equivalent DEM simulations were now performed using the rough crushable model (Fig. 12). In these simulations, the same parameters as in the oedometer test were used. Two sets of DEM simulations are presented: one with rough particles but crushing disabled, the other with rough particles and crushing activated. As expected the feature

Table 5
Experimental measurements of both particle limit force and roughness.

Source	Sand*	Mineralogy	N°	d_{av}/mm	$F_{lim,\ av}$/N	C_v^{**} (F_{lim})	F-δ *curve*	S_q/μm	C_v^{**} (S_q)
Cavarretta et al (2010)	LBS	Silica	1	1.67	> 60	–	Yes	0.3	–
McDowell (2002)	LBS	Silica	30	2	148.45	0.39	No	0.42 (Yao et al 2018)	0.13
Zhang et al (2020)	LBS	Silica	30	1.745	113	–	No	0.42 (Yao et al 2018)	0.13
Cil and Alshibli (2012)	OS	Silica	87	0.8	78.5	0.41	Yes	0.109 (Altuhafi et al 2016)	–
Nardelli et al (2017)	ES (black)	Silica	40	1.4	62.8	0.50	Yes	0.54	0.13
Nardelli et al (2017)	ES (pink)	Silica	40	1.34	47.9	0.55	Yes	0.28	0.57
Nardelli et al (2017)	ES (white)	Silica	40	1.55	59.8	0.39	Yes	0.69	0.17
Nardelli et al (2017)	ES (transparent)	Silica	40	1.52	131.6	0.53	Yes	0.59	0.12
Zhang et al (2020)	CDG	Mica, feldspar	30	1.805	48.7	–	No	1.34 (Sandeep and Senetakis 2018)	0.29
Zhang et al (2020)	CS	Corals, mol-lusc shells and algae	30	1.63	71.9	–	No	0.51 (Nardelli and Coop 2016)	0.24

* LBS - Leighton buzzard sand; OS - Ottawa sand; ES - Eglin sand; CDG - Completely decomposed granite; CD - Carbonate sand.
** C_v = coefficient of variation (Stdv/mean).

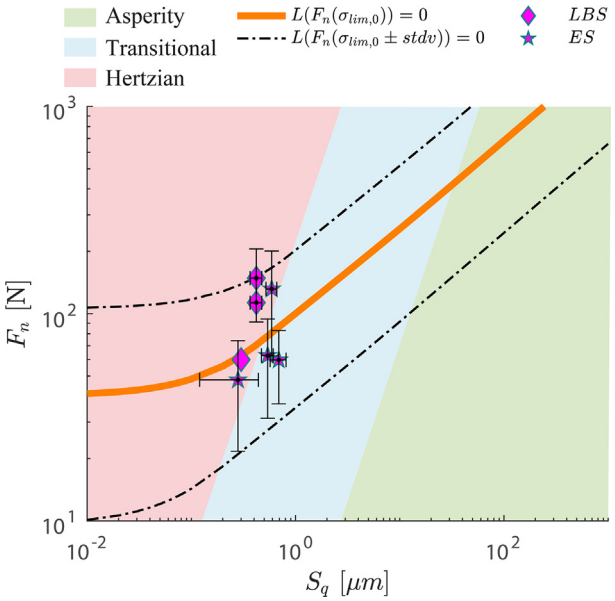

Fig. 10. Calibrated failure criteria ($d = 1.75$ mm) and experimental data of single particle crushing tests from literature on silica sand grains (1.5 mm $< d <$ 2 mm). Both theoretical and experimental data report variability in terms strength. Variability of S_q is reported only for the experimental data.

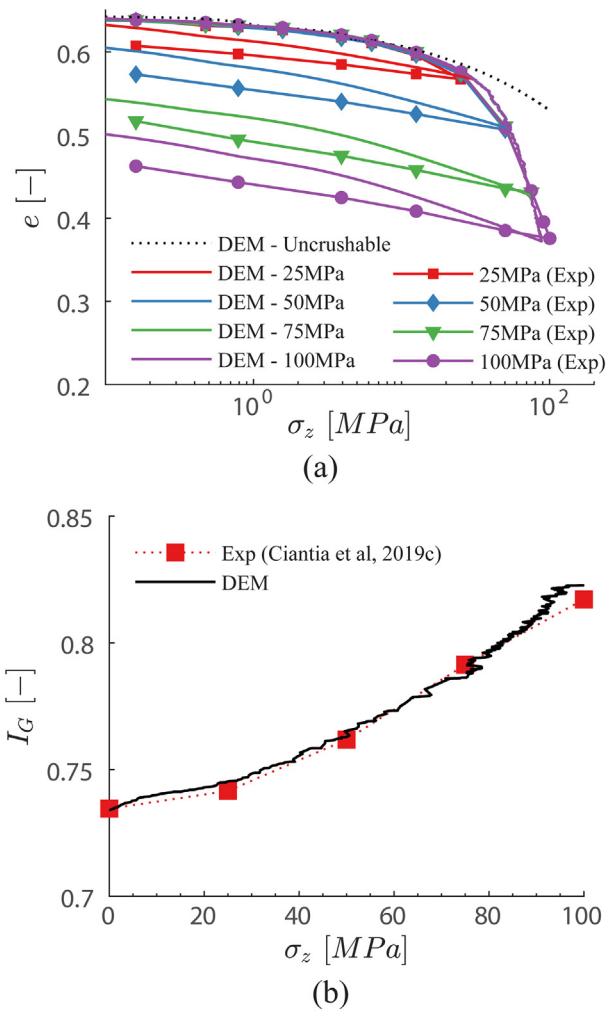

Fig. 11. Validation of crushing embedded in rough contact model via DEM simulation of high pressure oedometric compression tests in terms of (a) effective vertical stress vs void ratio in loading-unloading and (b) grading index evolution.

that is more relevant for this kind of high stress shearing test is crushability and not roughness: when crushing is disabled the brittle to ductile stress induced transition shown by the experiments is not present. On the other hand, when crushing is allowed, the rough crushable model reproduces well the experimental pattern.

It is also interesting to consider these triaxial responses from a micromechanical perspective. Fig. 13 presents the evolution of the mechanical coordination number Z^m during the triaxial compression tests simulated with the rough crushable model. Z^m was defined by Thornton (2000) as the coordination number computed after excluding particles with only one or no contacts.

In Fig. 13(a), the evolution of Z^m up to critical state (CS) is plotted against mean effective stress p. At critical states results from the rough crushable materials join a unique relation between Z^m and p, independent of grading, that was obtained by Ciantia et al. (2019c) using the smooth crushable model.

Note that the magnitude of reduction of Z^m decreases with the increase of initial confining pressure. As the triaxial path starts moving towards the critical state, the value of the mechanical coordination number Z^m falls abruptly and the fall is enhanced by dilatancy. Such abrupt falls in Z^m have been documented before in tests with dilatant responses (Gu et al., 2014). The onset of crushing reduces dilatancy and, therefore, also dampens the fall in coordination number, as witnessed by the test sheared at higher confinement in Fig. 13(b).

5. Discussion

The refined crushing model using measurable surface roughness achieves a more complete consideration of soil characteristics and is able to solve the difficulties encountered in the DEM simulations of simple tests for a representative silica sand. However, in the simulations presented all the particles have been assigned a unique roughness value. This is not realistic as the experimental data indicate a significant variability in roughness measurements, with coefficients of variation (Standard deviation / mean) around 0.5.

To explore this issue the numerical oedometer on the rough crushable Fontainebleau model was run again, but now roughness was assigned randomly according to a log-normal distribution of mean value 0.6 μm and standard

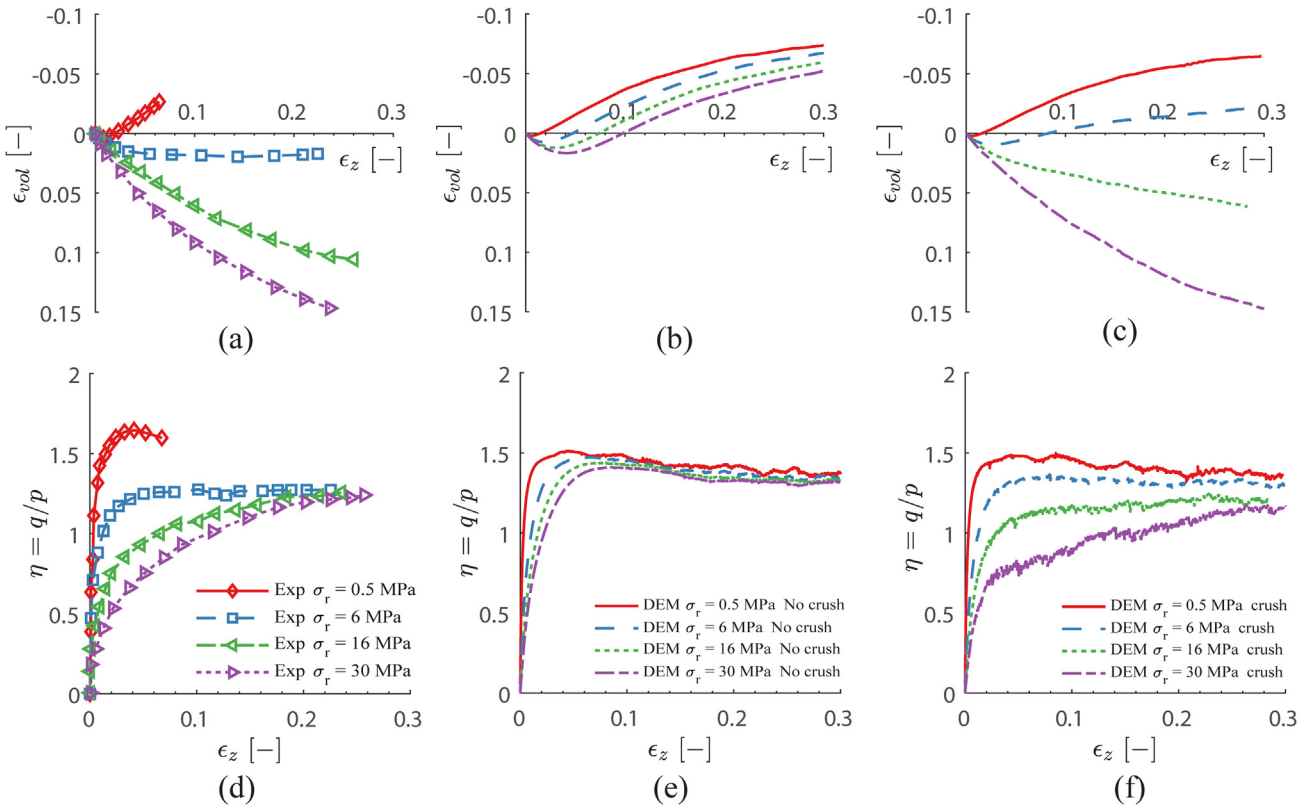

Fig. 12. DEM rough particle crushing model validation: high-confinement-pressure drained triaxial compression tests by Luong and Touati (1983) were simulated: (a) experimental; (b) numerical without crushing; (c) with crushing volumetric response; (d) experimental; (e) numerical without crushing; (f) with crushing stress–strain response.

deviation 0.3 μm. The variable roughness model showed earlier yielding (Fig. 14a) than the constant roughness one. This result indicates that roughness variability should be taken into account. However, it is not necessary to do so explicitly, as in this model the effect of particle roughness variability is already implicitly represented through particle strength variability.

There are two arguments that make plausible that implicit representation. First, the macroscopic effect just noted is the same effect observed by Ciantia et al. (2014) when the variability in particle crushing was increased. Second, the magnitude of crushing variability in the model is large enough to contain the effect of roughness variability.

Crushing variability is represented by the parameter *var*, coefficient of variation of particle strength at the reference size (2 mm). As indicated in Table 4, this was assigned a value of 0.36–0.38 based on results from single particle crushing tests (Ciantia et al., 2019c). It is possible to evaluate analytically the effect of the assumed roughness variability on the breakage force of 2 mm spheres. The result, illustrated in Fig. 14b is a breakage force distribution having a coefficient of variation of 0.1, which is well below the value given to *var*. The difference is due to other important factors affecting single particle crushing test results, like larger-scale shape features (e.g. sphericity and roundness) and orientation of particles (Wang and Arson, 2016; Tedesco et al., 2019). How to combine these different basic features with roughness in other DEM models might be an interesting topic for further study.

6. Conclusions

This contribution documents the incorporation of particle surface roughness into a DEM model for crushable sands. The effect of contact roughness on single particle breakage has been investigated via parametric studies. The model parameters for a discrete analogue of a representative quartz sand have been recalibrated. The main findings are:

- The parametric study shows that increasing either roughness or the n_i ratios results in larger crushing forces and less stiff contact behaviour;
- The effect of roughness S_q is more significative than those of the n_i ratios. Generally, for relatively small roughness values, ($S_q < 0.1$ μm), the crushing force F_{lim} is independent of roughness, while with the increase of roughness ($S_q > 0.1$ μm) the crushing force F_{lim} increases significantly. The failure takes place in the transition regime or even (for $S_q > 20$ μm) in the asperity-dominated contact regime;

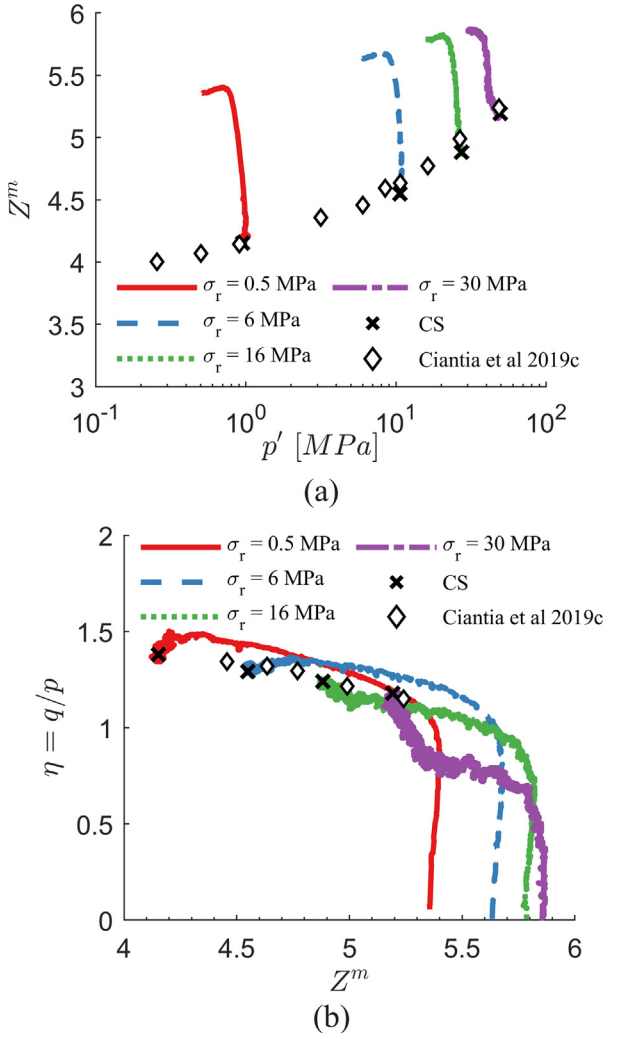

Fig. 13. Relation between mechanical coordination number Z^m and (a) mean pressure (b) stress ratio, during the triaxial compression tests on rough-crushable material of Fig. 12.

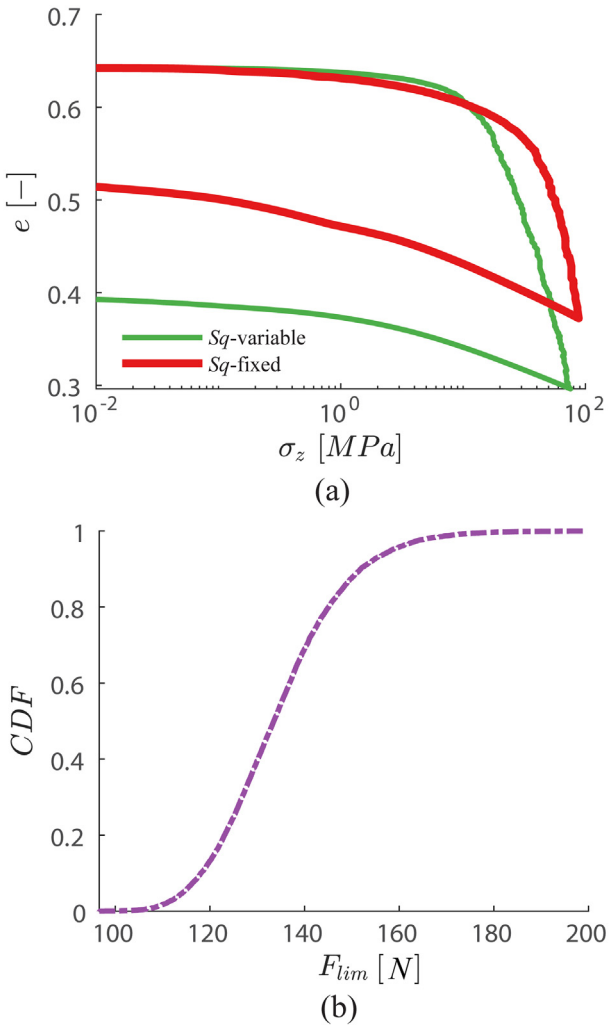

Fig. 14. Effect of roughness variability on (a) macroscopic response of 1D compression test (b) cumulative distribution function (CDF) of a 2 mm diameter particle breakage force.

- Comparing experimental data from literature and the newly developed contact model, suggests that crushing of silica sand grains of diameter 1.5 mm $< d <$ 2 mm is unlikely to happen in the roughness dominated region but would rather occur in the Hertzian contact regime.
- The effect of contact roughness on limiting strength does not show much dependency on particle sizes;
- The recalibrated parameters including realistic values of surface roughness (using realistic values of elastic bulk properties for the sand grains) enable to correctly capture both load-unload behaviour and particle size distribution evolution of high pressure oedometric tests. Roughness is then a model refinement that may result in simpler and more objective DEM calibrations which can then feed into constitutive model for crushable soils (e.g. Kikumoto et al., 2010).

Acknowledgements

This work was partly supported by the Ministry of Science and Innovation of Spain through the research grant BIA2017-84752-R and by the EPCC-CIRRUS Scottish Academic Access sc019-EPCC-CIRRUS project.

Appendix A. Establishment of crushing criterion

An expression for normal stiffness can be obtained by differentiating F_n with respect to δ in Eq. (1),

$$k_n = \left(6E'^2 r' F_n\right)^{1/3} \tag{21}$$

Following Otsubo et al. (2015) the shear stiffness is taken as

$$k_s = \frac{2(1-v)}{2-v} k_n \tag{22}$$

Recall that the expressions for the threshold forces in the rough contact model, F_{nT1} and F_{nT2} are given by

$$F_{nT1} = S_q E' \sqrt{2r' S_q} \tag{4bis}$$

$$F_{nT2} = 100 F_{nT1} \tag{5bis}$$

To these threshold forces correspond threshold displacements δ_{T1} and δ_{T2} given by

$$\delta_{T2} = \left(\frac{3F_{nT2}}{4E'\sqrt{r'}}\right)^{2/3} + \delta_1 + \delta_2 \tag{23}$$

$$\delta_{T1} = \left(\frac{F_{nT1}}{F_{nT2}}\right)^{1/b} (\delta_{T2} - \delta_1) + \delta_1 \tag{24}$$

Where b and c are constants chosen to ensure continuity at the transition points of the F_n-δ regimes and given by

$$b = 1.5 * \left(1 + \frac{\delta_2}{\delta_{T2} - \delta_1 - \delta_2}\right) \tag{25}$$

$$c = 100 b \delta_{T1} \frac{(\delta_{T1} - \delta_1)^{b-1}}{(\delta_{T2} - \delta_1)^b} \tag{26}$$

Rearranging Eqs. (6)–(8), expressions for the contact overlap are obtained for all possible values of F_n, covering the three contact regimes. In the asperity-dominated regime, when $F_n < F_{nT1}$

$$\delta = \left(\frac{F_n}{F_{nT1}}\right)^{\frac{1}{c}} \delta_{T1} \tag{27}$$

In the transitional regime, when $F_{nT1} \le F_n < F_{nT2}$

$$\delta = \left(\frac{F_n}{F_{nT2}}\right)^{\frac{1}{b}} (\delta_{T2} - \delta_1) + \delta_1 \tag{28}$$

And in the Hertzian regime, when $F_{nT2} \le F_n$

$$\delta = \left(\frac{9F_n^2}{16E'^2 r'}\right)^{\frac{1}{3}} + \delta_1 + \delta_2 \tag{29}$$

Combining Eqs. (13), (14), (15) and (16) a generic limit expression for the normal contact force is obtained as

$$F_n \leqslant \sigma_{\lim,0} f(var) \left(\frac{d}{d_0}\right)^{-3/m} \pi r' \delta \tag{30}$$

In which the expressions for contact overlap (27)-(29) appropriate to each contact regime are substituted to obtain three different expression for the limit normal contact force. In the asperity-dominated regime, when Fn $< F_{nT1}$

$$F_n \leqslant \sigma_{\lim,0} f(var) \left(\frac{d}{d_0}\right)^{-\frac{3}{m}} \pi r' \left(\frac{F_n}{S_q E' \sqrt{2r' S_q}}\right)$$
$$\frac{1}{c}\left\{\left(\frac{1}{100}\right)^{\frac{1}{b}}\left[\left(\frac{300 S_q E' \sqrt{2r' S_q}}{4E'\sqrt{r'}}\right)^{\frac{2}{3}} + n_2 S_q\right] + n_1 S_q\right\} \tag{31}$$

In the transitional regime, when $F_{nT1} \le F_n < F_{nT2}$

$$F_n \leqslant \sigma_{\lim,0} f(var) \left(\frac{d}{d_0}\right)^{-\frac{3}{m}} \pi r'$$
$$\left\{\left(\frac{F_n}{100 S_q E' \sqrt{2r' S_q}}\right)^{\frac{1}{b}}\left[\left(\frac{300 S_q E' \sqrt{2r' S_q}}{4E'\sqrt{r'}}\right)^{\frac{2}{3}} + n_2 S_q\right] + n_1 S_q\right\} \tag{32}$$

And in the Hertzian regime, when $F_{nT2} \le F_n$

$$F_n \le \sigma_{lim,0} f(var) \left(\frac{d}{d_0}\right)^{-\frac{3}{m}} \pi r' \left[\left(\frac{9F_n^2}{16E'^2 r'}\right)^{\frac{1}{3}} + n_1 S_q + n_2 S_q\right] \tag{33}$$

References

Alshibli, K.A., Alsaleh, M.I., 2004. Characterizing surface roughness and shape of sands using digital microscopy. J. Comput. Civil Eng. 18 (1), 36–45. https://doi.org/10.1061/(ASCE)0887-3801(2004)18.

Altuhafi, F.N., Coop, M.R., Georgiannou, V.N., 2016. Effect of particle shape on the mechanical behavior of natural sands. J. Geotech. Geoenviron. Eng. 142 (12). https://doi.org/10.1061/(ASCE)GT.1943-5606.0001569.

Barret, P.J., 1980. The shape of rock particle, a critical review. Sedimentology 27, 291–303. https://doi.org/10.1111/j.1365-3091.1980.tb01179.x.

Butlanska, J., Arroyo, M., Amoroso, S., Gens, A., 2018. Marchetti flat dilatometer tests in a virtual calibration chamber. Geotech. Test. J. 41 (5), 930–945.

Cavarretta, I., Coop, M., O'Sullivan, C., 2010. The influence of particle characteristics on the behaviour of coarse grained soils. Géotechnique 60 (6), 413–423. https://doi.org/10.1680/geot.2010.60.6.413.

Chaudry, M.A., Woitzik, C., Düster, A., Wriggers, P., 2018. Experimental and numerical characterization of expanded glass granules. Comput. Part. Mech. 5 (3), 297–312. https://doi.org/10.1007/s40571-017-0169-0.

Christensen, R.M., 2000. Yield functions, damage states, and intrinsic strength. Math. Mech. Solids 5 (3), 285–300.

Ciantia, M., O'Sullivan, C., 2020. Calculating the state parameter in crushable sands. Int. J. Geomech. https://doi.org/10.1061/(ASCE)GM.1943-5622.0001707.

Ciantia, M., O'Sullivan, C., Jardine, R.J., 2019a. Pile penetration in crushable soils: Insights from micromechanical modelling. 17th European Conference on soil Mechanics and Geotechnical Engineering (ECSMGE 2019). International Society for Soil Mechanics and Geotechnical Engineering, pp. 298–317.

Ciantia, M.O., Arroyo, M., O'Sullivan, C., Gens, A., 2019b. Micromechanical Inspection of Incremental Behaviour of Crushable Soils. Acta Geotech. 14 (5), 1337–1356. https://doi.org/10.1007/s11440-019-00802-0.

Ciantia, M.O., Arroyo, M., O'Sullivan, C., Gens, A., Liu, T., 2019c. Grading evolution and critical state in a discrete numerical model of Fontainebleau sand. Géotechnique 69 (1), 1–15. https://doi.org/10.1680/jgeot.17.P.023.

Ciantia, M., Zhang, N., Arroyo, M., 2017. Enhancing Efficiency of DEM Modeling of Particle Breakage. In: 25th UKACM Conference on Computational Mechanics. Birmingham.

Ciantia, M.O., Arroyo, M., Butlanska, J., Gens, A., 2016. DEM modelling of cone penetration tests in a double-porosity crushable granular material. Comput. Geotech. 73, 109–127.

Ciantia, M.O., Arroyo, M., Calvetti, F., Gens, A., 2015. An approach to enhance efficiency of DEM modelling of soils with crushable grains. Geótechnique 65, 91–110.
Ciantia, M.O., Arroyo, M., Gens, A., Calvetti, F., 2014. Particle failure in DEM models of crushable soil response. In: Hicks, M.A., Brinkgreve, R.B.J., Rohe, A. (Eds.), Numerical Methods in Geotechnical Engineering. CRC Press/Balkema, Leiden, the Netherlands, pp. 345–350.
Cil, M.B., Alshibli, K.A., 2012. 3D assessment of fracture of sand particles using discrete element method. Géotech. Lett. 2 (3), 161–166. https://doi.org/10.1680/geolett.12.00024.
Coetzee, C.J., 2016. Calibration of the discrete element method and the effect of particle shape. Powder Technol. 297, 50–70.
De Bono, J.P., McDowell, G.R., 2014. DEM of triaxial tests on crushable sand. Granular Matter 16 (4), 551–562.
De Bono, J.P., McDowell, G.R., 2018. Micro mechanics of drained and undrained shearing of compacted and overconsolidated crushable sand. Geotechnique 68, 575–589. https://doi.org/10.1680/jgeot.16.P.318.
Garcia, F.E., Bray, J.D., 2018. Distinct element simulations of earthquake fault rupture through materials of varying density. Soils Found. 58 (4), 986–1000.
Greenwood, J.A., Tripp, J.H., 1967. The elastic contact of rough spheres. J. Appl. Mech. 34 (1), 153–159.
Gu, X., Huang, M., Qian, J., 2014. DEM investigation on the evolution of microstructure in granular soils under shearing. Granular Matter 16, 91–106. https://doi.org/10.1007/s10035-013-0467-z.
Einav, I., 2007. Breakage mechanics-Part I: Theory. J. Mech. Phys. Solids 55, 1274–1297.
Fu, R., Hu, X., Zhou, B., 2017. Discrete element modeling of crushable sands considering realistic particle shape effect. Comput. Geotech. 91, 179–191.
Hanley, K.J., O'Sullivan, C., Huang, X., 2015. Particle-scale mechanics of sand crushing in compression and shearing using DEM. Soils Found. 55 (5), 1100–1112.
Harkness, J., Zervos, A., Le Pen, L., Aingaran, S., Powrie, W., 2016. Discrete element simulation of railway ballast: modelling cell pressure effects in triaxial tests. Granular Matter 18 (3), 65.
Irazábal, J., Salazar, F., Oñate, E., 2017. Numerical modelling of granular materials with spherical discrete particles and the bounded rolling friction model. Application to railway ballast. Comput. Geotech. 85, 220–229. https://doi.org/10.1016/j.compgeo.2016.12.034.
ISO 14688-1, 2017. Geotechnical investigation and testing – Identification and classification of soil – Part 1: Identification and description
Itasca, 2017. PFC – particle flow code, ver. 5.0. Minneapolis, MN, USA: Itasca Consulting Group.
Kawano, K., Shire, T., O'Sullivan, C., 2018. Coupled particle-fluid simulations of the initiation of suffusion. Soils Found. 58 (4), 972–985.
Kikumoto, M., Wood, D.M., Russell, A., 2010. Particle crushing and deformation behaviour. Soils Found. 50 (4), 547–563.
Liu, S., Wang, J., Kwok, C.Y., 2019. DEM simulation of creep in one-dimensional compression of crushable sand. J. Geotech. Geoenviron. Eng. 145 (10), 04019060.
Lobo-Guerrero, S., Vallejo, L.E., 2005. DEM analysis of crushing around driven piles in granular materials. Géotechnique 55 (8), 617–623.
Luong, M.P., Touati, A., 1983. Sols Grenus Sous Fortes Contraintes. Rev. Fr. Geotech. 24, 51–63.
Ma, G., Chen, Y., Yao, F., Zhou, W., Wang, Q., 2019. Evolution of particle size and shape towards a steady state: Insights from FDEM simulations of crushable granular materials. Comput. Geotech. 112, 147–158.
McDowell, G.R., 2002. On the Yielding and Plastic Compression of Sand. Soils Found. 42, 139–145. https://doi.org/10.3208/sandf.42.139.
McDowell, G.R., De Bono, J.P., 2013. On the micro mechanics of one-dimensional normal compression. Géotechnique, 63, 895–908.
Muir Wood, D., 2007. The magic of sands — The 20th Bjerrum Lecture presented in Oslo, 25 November 2005. Can. Geotech. J. 44, 1329–1350.
Nadimi, S., Ghanbarzadeh, A., Neville, A., Ghadiri, M., 2019. Effect of particle roughness on the bulk deformation using coupled boundary element and discrete element methods. Comput. Part. Mech., (0123456789). 10.1007/s40571-019-00288-3.
Nakata, A.F.L., Hyde, M., Hyodo, H., Murata, 1999. A probabilistic approach to sand particle crushing in the triaxial test. Géotechnique, 49(5), 567-583.
Nakata, Y., Hyodo, M., Hyde, A. F., Kato, Y., Murata, H., 2001. Microscopic particle crushing of sand subjected to high pressure one-dimensional compression. Soils Found., 41, No. 1, 69–82.
Nardelli, Vincenzo, Coop, M.R., 2016. The micromechanical behaviour of a biogenic carbonate sand. Proc. Eng. 158, 39–44. https://doi.org/10.1016/j.proeng.2016.08.402.
Nardelli, V., Coop, M.R., Andrade, J.E., Paccagnella, F., 2017. An experimental investigation of the micromechanics of Eglin sand. Powder Technol. 312, 166–174. https://doi.org/10.1016/j.powtec.2017.02.009.
Nardelli, V., Coop, M.R., 2019. The experimental contact behaviour of natural sands: normal and tangential loading. Geótechnique 69 (8), 672–686. https://doi.org/10.1680/jgeot.17.P.167.
Otsubo, M., O'Sullivan, C., 2018. Experimental and DEM assessment of the stress-dependency of surface roughness effects on shear modulus. Soils Found. 58, 602–614.
Otsubo, M., O'Sullivan, C., Hanley, K.J., Sim, W.W., 2017. The influence of particle surface roughness on elastic stiffness and dynamic response. Géotechnique 67, 452–459.
Otsubo, M., O'sullivan, C., Shire, T., 2017b. Empirical assessment of the critical time increment in explicit particulate discrete element method simulations. Comput. Geotech., 86, 67–79.
Otsubo, M., O'sullivan, C., Sim, W.W., Ibraim, E., 2015. Quantitative assessment of the influence of surface roughness on soil stiffness. Géotechnique, 65, 694–700.
Rorato, R., Arroyo, M., Gens, A., Andò, E., Viggiani, G., 2021. Image-based calibration of rolling resistance in discrete element models of sand. Computers and Geotechnics 131, 103929.
Russell, A.R., Muir Wood, D., Kikumoto, M., 2009. Crushing of particles in idealised granular assemblies. J. Mech. Phys. Solids 57 (8), 1293–1313.
Salazar, A., Sáez, E., Pardo, G., 2015. Modeling the direct shear test of a coarse sand using the 3D Discrete Element Method with a rolling friction model. Comput. Geotech. 67, 83–93. https://doi.org/10.1016/j.compgeo.2015.02.017.
Sandeep, C.S., Senetakis, K., 2018. Effect of young's modulus and surface roughness on the inter-particle friction of granular materials. Materials 11 (2). https://doi.org/10.3390/ma11020217.
Santamarina, C., Cascante, G., 1998. Effect of surface roughness on wave propagation parameters. Geotechnique 48 (1), 129–136.
Senetakis, K., Coop, M.R., Todisco, M.C., 2013. The inter-particle coefficient of friction at the contacts of Leighton Buzzard sand quartz minerals. Soils Found. 53 (5), 746–755.
Sharifipour, M., Dano, C., 2006. Effect of grains roughness on waves velocities in granular packings. Proceedings of the 1st Euro Mediterranean conference on advances on geomaterials and structure. Hammamet, pp. 123–128.
Shen, Z., Jiang, M., Wang, S., 2019. Static and kinematic damage characterization in structured sand. Acta Geotech. 14 (5), 1403–1421.
Tamura, S., Higuchi, Y., Hayashi, Y., Yamzasaki, M., 2012. Centrifuge studies on the effects of existing piles on the end resistance and shaft friction of a new pile. Soils Found. 52 (6), 1062–1072.
Tedesco, B., Neto, M.P.C., Tarantino, A., Farias, M., 2019. Design of crushable particles in DEM based on single grain compression. In: E3S Web of Conferences (Vol. 92, p. 14005). EDP Sciences.
Thornton, C., 2000. Numerical simulations of deviatoric shear deformation of granular media. Géotechnique 50 (1), 43–53. https://doi.org/10.1680/geot.2000.50.1.43.
Thornton, C., 2015. Granular Dynamics Contact Mechanics and Particle System Simulations: a DEM study. Springer, Part. Technol. Ser. 24. https://doi.org/10.1007/978-3-319-18711-2_3.

Wang, P., Karatza, Z., Arson, C., 2019. DEM modelling of sequential fragmentation of zeolite granules under oedometric compression based on XCT observations. Powder Technol. 347, 66–75.

Wang, P., Arson, C., 2018. Energy distribution during the quasi-static confined comminution of granular materials. Acta Geotech. 13 (5), 1075–1083.

Wang, P., Arson, C., 2016. Discrete element modeling of shielding and size effects during single particle crushing. Comput. Geotech. 78, 227–236.

Wang, R., Fu, P., Zhang, J.M., Dafalias, Y.F., 2016. DEM study of fabric features governing undrained post-liquefaction shear deformation of sand. Acta Geotech. 11 (6), 1321–1337.

Xu, X.m., Ling, D.s., Cheng, Y.p., Chen, Y.m., 2015. Correlation between liquefaction resistance and shear wave velocity of granular soils: a micromechanical perspective. Géotechnique, 65(5), 337–348. 10.1680/geot.SIP.15.P.022.

Yang, Z.X., Jardine, R.J., Zhu, B.T., Rimoy, S., 2014. Stresses Developed around Displacement Piles Penetration in Sand. J. Geotech. Geoenviron. Eng. 140, 04013027.

Yao, T., Baudet, B.A., Lourenço, S.D.N., 2018. Quantification of the surface roughness of quartz sand using optical interferometry. Meccanica, 1–8.

Zhang, N., Arroyo, M., Ciantia, M.O., Gens, A., Butlanska, J., 2019. Standard penetration testing in a virtual calibration chamber. Comput. Geotech. 111, 277–289.

Zhang, N., Arroyo, M., Ciantia, M.O., Gens, A., 2021. Energy balance analyses during Standard Penetration Tests in a Virtual Calibration Chamber. Computers and Geotechnics 133, 104040.

Zhang, N., Evans, T.M., 2018. Three dimensional discrete element method simulations of interface shear. Soils Found. 58 (4), 941–956.

Zhang, X., Baudet, B.A., Yao, T., 2020. The influence of particle shape and mineralogy on the particle strength, breakage and compressibility. Int. J. Geo-Eng. 11 (1), 4–13. https://doi.org/10.1186/s40703-020-0108-4.

Zhao, B., Wang, J., Coop, M.R., Viggiani, G., Jiang, M., 2015. An investigation of single sand particle fracture using X-ray microtomography. Géotechnique 65, 625–641. https://doi.org/10.1680/geot.4.P.157.

Zhao, T., Feng, Y.T., Wang, M., 2018. An extended Greenwood-Williamson model based normal interaction law for discrete element modelling of spherical particles with surface roughness. Int. J. Numer. Anal. Meth. Geomech. 42 (14), 1624–1642.

Zhou, W., Wang, D., Ma, G., Cao, X., Hu, C., Wu, W., 2020. Discrete element modeling of particle breakage considering different fragment replacement modes. Powder Technol. 360, 312–323. https://doi.org/10.1016/j.powtec.2019.10.002.